Brell, M., Segl, K., Guanter, L., Bookhagen, B. (2019): 3D hyperspectral point cloud generation: Fusing airborne laser scanning and hyperspectral imaging sensors for improved object-based information extraction. - *ISPRS Journal of Photogrammetry and Remote Sensing*, *149*, pp. 200—214.

DOI: http://doi.org/10.1016/j.isprsjprs.2019.01.022

3D hyperspectral point cloud generation: fusing airborne laser scanning and hyperspectral imaging sensors for improved object-based information extraction

Maximilian Brell[1,*], Karl Segl[1], Luis Guanter[1], Bodo Bookhagen[2]

1. Helmholtz Centre Potsdam–GFZ German Research Centre for Geosciences, Section 1.4 Remote Sensing, Telegrafenberg, 14473 Potsdam, Germany; E-mails: maximilian.brell@gfz-potsdam.de (M.B.), karl.segl@gfz-potsdam.de (K.S.), and luis.guanter@gfz-potsdam.de (L.G.)

2. University of Potsdam, Institute of Earth and Environmental Science, Karl-Liebknecht-Str. 24-25, 14476 Potsdam, Germany; E-mail: Bodo.Bookhagen@uni-potsdam.de (B.B.)

* Corresponding author; E-mail: maximilian.brell@gfz-potsdam.de;
Tel.: +49-331-288-1195; Fax: +49-331-288-1192.

Abstract

Remote Sensing technologies allow to map biophysical, biochemical, and earth surface parameters of the land surface. Of especial interest for various applications in environmental and urban sciences is the combination of spectral and 3D elevation information. However, those two data streams are provided separately by different instruments, namely airborne laser scanner (ALS) for elevation and a hyperspectral imager (HSI) for high spectral resolution data. The fusion of ALS and HSI data can thus lead to a single data entity consistently featuring rich structural and spectral information. In this study, we present the application of fusing the first pulse return information from ALS data at a sub-decimeter spatial resolution with the lower-spatial resolution hyperspectral information available from the HSI into a hyperspectral point cloud (HSPC). During the processing, a plausible hyperspectral spectrum is assigned to every first-return ALS point. We show that the complementary implementation of spectral and 3D information at the point-cloud scale improves object-based classification and information

extraction schemes. This improvements have great potential for numerous land-cover mapping and environmental applications.

Keywords: lidar; multispectral point cloud; laser return intensity; unmixing; sharpening; imaging spectroscopy; in-flight; pixel level; sensor fusion; data fusion; preprocessing; point cloud segmentation; semantic labeling

1 Introduction

The automated extraction of object-based information (OBI) from airborne remote sensing data as required in the environmental and earth sciences is challenging, especially for spectrally and spatially heterogeneous data. In general, the ability of remote sensing data to represent the complexity of any environment depends not only on the spatial and spectral resolution of the measurement, but also on the capacity to capture the 3D structural information. In recent years, the fusion of elevation information from light detection and ranging (lidar) especially airborne laser scanning (ALS) with hyperspectral image (HSI) data has demonstrated the potential to meet these advanced requirements (Asner et al., 2017, 2007; Dalponte et al., 2008; Eitel et al., 2016; Alonzo et al., 2014; Debes et al., 2014; Torabzadeh et al., 2014). Applications such as the identification of individual tree species, the estimation of forest biomass, and urban feature classification place enormous demands on the spectral, spatial and elevation information content of remotely sensed data (Cook et al., 2013; Kampe et al., 2009). All these studies indicate that the segmentation of three-dimensional elevation and spectral information into real-world objects is highly advantageous for object-based derivation of ecological, environmental, and earth surface parameters. Spectral and elevation variability, various height parameters, projected areas and volumes of objects are standard parameters, which are necessary for biophysical, biochemical and earth surface parameter estimation. For example, for a digital canopy model, the crown diameter, canopy height, and crown-base height can be derived from the elevation information of the point cloud (e.g. Morsdorf et al., 2003; Holmgren and Persson, 2004; Dalponte et al., 2014). However, individual tree type and species classifications (Clark et al., 2005; Alonzo et al., 2014; Dalponte et al., 2014), as well as vitality estimations, can be improved by spectral information. Furthermore, the combination of spectral and structure information is not only beneficial for forest biomass mapping, but also for urban mapping (Man et al., 2015; Heiden et al., 2012; Alonzo et al., 2014) where the degree of soil sealing, plant structure, roof material and roughness of specific surface material are valuable pieces of information. Therefore, environmental applications at local to regional scales will benefit from an improved object-based parameter estimation.

Object-based parameter estimation can thus greatly benefit from the combination of elevation and spectral information, which motivates the development of methods to fuse ALS and HSI data. In general, the generation of hyperspectral point clouds can be distinguished into 3 main categories. First, the real physical measurement approaches based on hyperspectral lidar sensor systems (Hakala et al., 2012; Vauhkonen et al., 2013). Second, the generation based on HSI and lidar sensor fusion (Buckley et al., 2013; Buddenbaum et al., 2013; Dalponte et al., 2008, 2012; Debes et al., 2014; Sankey et al., 2017; Suomalainen et al., 2011) and third, the generation based on photogrammetric range imaging techniques (Oliveira et al., 2019; Aasen et al., 2015; Näsi et al., 2015; Nevalainen et al., 2017). In operational and quality terms, a single airborne sensor system is not capable of complying with all these demands. Multi-sensor solutions such as ALS and HSI are available, but their spatial and spectral alignment is challenging due to different sampling strategies, interaction with surface objects, and fundamentally different sensor characteristics (Brell et al., 2017, 2016). The resulting different spatial ground sampling patterns, as well as diverse spectral behavior and interaction with surface objects, result in a discretization of the relatively coarse spatial resolution of the HSI sensor with a fall back to spatially degraded pseudo-3D (2.5D) grid information. However, a pixel-based representation is often not sufficient, because valuable structural and also spectral information are lost, and it often does not represent the necessary details of the environment and thus the appropriate application feature level. HSI measurements especially for heterogeneous areas such as forests (Clasen et al., 2015; Dandois and Ellis, 2013) or urban areas (Alonzo et al., 2015; Heiden et al., 2012; Roessner et al., 2001) are discretized unfortunately in a mixed HSI pixel (Roberts et al., 1998; Bioucas-Dias et al., 2012). Especially for biomass estimation, the ALS metric is extremely valuable. Single tree detection, tree species, tree height, canopy density, and crown size are sensitive parameters for biomass estimation (Anderson et al., 2008; Clark et al., 2011; Asner et al., 2017; Alonzo et al., 2014; Dalponte et al., 2008; Morsdorf et al., 2006; Luo et al., 2017). Moreover, earth surface parameters such as surface roughness or texture for a certain soil type or surface sealing are advantageous for runoff, erosion and other mass movement estimations (Eitel et al., 2016). However, the expansion of 3D mapping capabilities with adequate spectral information to measure spectral and structural properties simultaneously has not been fulfilled yet and a selective OBI extraction is still limited. One approach to satisfy the need of combined elevation ALS and spectral HSI information is to upgrade the point cloud provided by the ALS with hyperspectral information, while preserving its original spatial resolution, irregular and full 3D characteristics. In this work, we present an application of a new fusion method, which allocates appropriate spectra to the first-return ALS points. Our method aims to synergistically combine the highest possible 3D and spectral resolution information in one comprehensive 3D hyperspectral point cloud (HSPC) data entity. This manuscripts introduces a method to generate HSPC data from separate HSI and ALS data streams and evaluates the potential of such a data entity for advanced land cover mapping applications. We show that the resulting HSPC is more appropriate for OBI extraction because it combines spectral and structural information at the point cloud level in a consistent manner.

2 General aspects of HSI and ALS data fusion

We strive to enable a comprehensive OBI extraction from a homogeneous spectral and point-cloud data domain for various environmental and urban applications. The overall concept of the HSPC is illustrated in Fig. 1, showing the properties of each data entity.

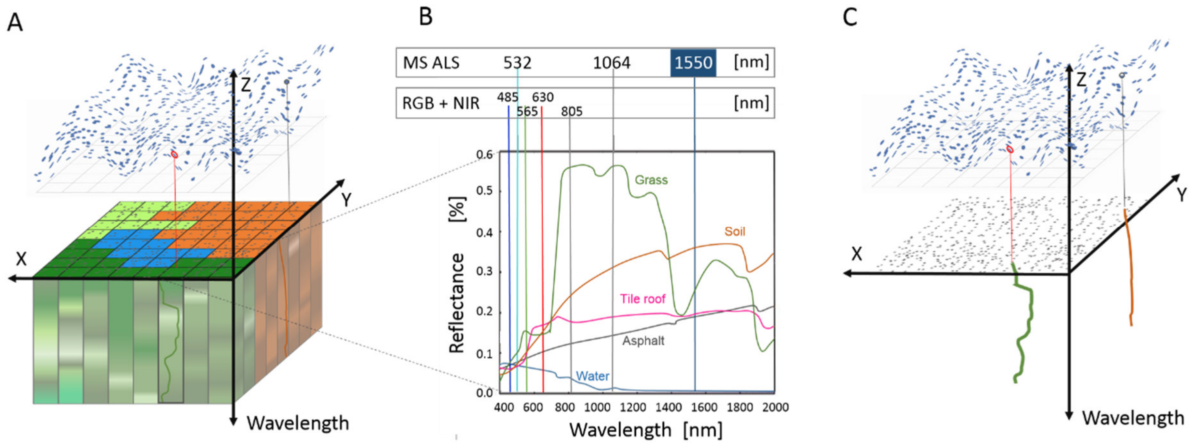

Fig. 1: Concept of the hyperspectral point cloud (HSPC). (A) ALS point cloud (first returns) versus an HSI data cube. (B) Spectral overlap between HSI and the ALS sensor at 1550 nm; other common ALS wavelengths such as 1064 and 532 nm and potential overlaps with alternative sensors like multispectral (MS) ALS and an aerial camera (RGB+ NIR) are also depicted. (C) Conceptual view of the fused HSPC where the spectrum for two points is shown.

For the generation of an HSPC and the subsequent OBI extraction, some basic considerations are important. The spatial resolution of the HSI is typically lower than that of the ALS. In contrast, actively sensing ALS systems can provide very high spatial resolution elevation and intensity information (Fig. 1), but presently for only one wavelength, which overlaps with the HSI data cube. These contrasting sensor characteristics and data entities cause the main problems and challenges for a fusion of airborne ALS and HSI data. However, the exploitation of the active illumination of lidar inside the fusion process can overcome these drawbacks. It can be used for geometric co-registration of the two sensors (Brell et al., 2016) and for correcting the HSI data for shadow, illumination, and anisotropic effects on a physical basis (Brell et al., 2017). To address the different spatial and spectral sensor responses of these two contrasting sensor, the assignment of HSI spectra to the ALS point cloud has to comprise spatial and spectral alignments, as well as the unmixing-based spectra assignment itself. Consequently, three pre-processing steps are necessary: First, ALS point cloud filtering to include only the first returns, which represent the primary surface that is measured by the HSI. Highly non-linear interactions of penetrable surfaces are not considered. Second, a radiometric calibration of the ALS intensity data which results in ALS bottom-of-atmosphere reflectance data (Briese et al., 2012; Kashani et al., 2015; Wagner, 2010). Third, the atmospherically correction of the HSI data into bottom-of-atmosphere reflectance (Guanter et al., 2009).

The simplest method to drape co-registered imagery over a point cloud is matching the nearest neighbor pixel to an XYZ point. This process is adequate for fusing data sets with a similar ground sampling distance. However, for fusing spatial coarse HSI data with a spatial dense point cloud, this nearest neighbor assignment (NNA) does not adequately represent the spectral characteristic at a given point.

A wide range of pansharpening approaches exist to address the problem of different spatial resolutions. In general, these approaches combine the high spatial resolution of a panchromatic image with a lower resolution multispectral (MS) image (Thomas et al., 2008; Vivone et al., 2015). For fusing panchromatic images with HSI images, those approaches have been adapted to meet the demands of spatially enhancing high spectral resolution imaging (Loncan et al., 2015). The variety of methods corresponds to MS applications. Nevertheless, the small spectral overlap between the high spatial resolution band and the much wider spectral range of the HSI (400-2500 nm) limits a straight forward fusion of both data entities. The complexity of HSI and ALS data fusion is in general similar to pansharpening methods, but differs in three key aspects: First, only a very narrow wavelength range is covered by ALS intensity information inside the wide spectral HSI (400-2500 nm) range. Compared to a wide panchromatic or MS band, the single wavelength of the ALS information content is highly restricted. Second, the spectral contrast between various objects is poor in the recorded 1550 nm wavelength range. Third, the ALS point cloud is irregular and thus sporadically sparse. These three challenges have to be properly addressed for a proper fusion.

For HSI images the spatial resolution can be sharpened based on spatial dependent spectral unmixing. (Yokoya et al., 2012). Spectral unmixing is a commonly used method for calculating the fractions (called abundances) of pure materials (called endmembers) within a mixed pixel (Roberts et al., 1998; Bioucas-Dias et al., 2012). It is well known that too many or too few endmembers degrade the unmixing result. Additional information must be taken into account to prevent the selection of inappropriate and incorrect endmembers that do not influence a pixel of interest and to solve this ill-posed inverse problem. A widely used approach is the integration of spatial information for optimal endmember selection. The neighborhood and spatial context considerations are established in various unmixing studies (Roessner et al., 2001; Rogge et al., 2007, 2006). A more general overview of incorporating spatial information to unmixing is given in several studies (Gorretta and Gomez, 2016; Shi and Wang, 2014; Wang et al., 2016).

The preservation and enhancement of the spectral information content of the HSI data and the 3D character of the ALS data inside a HSPC is realized based on these considerations. Our fusion method considers the spectral and spatial neighborhood of the high spatial resolution ALS point cloud. A regularization is carried out by introducing complementary neighborhood and spatial context on a segment level. The goal is to group HSI pixels into segments with similar spectral characteristics and without any structural or spectral gradients. In this way, the HSI endmember set per segment can be optimized. The spectral variation within a segment is usually kept small. Per-segment endmember sets based on the spatial relationship between adjacent segments and the selection of the most representing endmembers for a certain segment can be provided by an adequate algorithm. Such a segmentation-based endmember selection serves as a controlling factor of the unmixing process. The number of endmembers used for unmixing a specific segment is reduced while considering the substantial variation of the endmembers composing such segments. All these basic considerations enable the HSPC generation described in the method part.

3 **Materials and Methods**

3.1 Hyperspectral point cloud generation

The fused HSPC is achieved by a segmentation-based spatial unmixing assignment (SSA), which extracts adequate spectra for every ALS point. The processing flow can be conceptually separated into input data generation and pre-processing and the production of the HSPC (Fig. 2), which are described in the next sections.

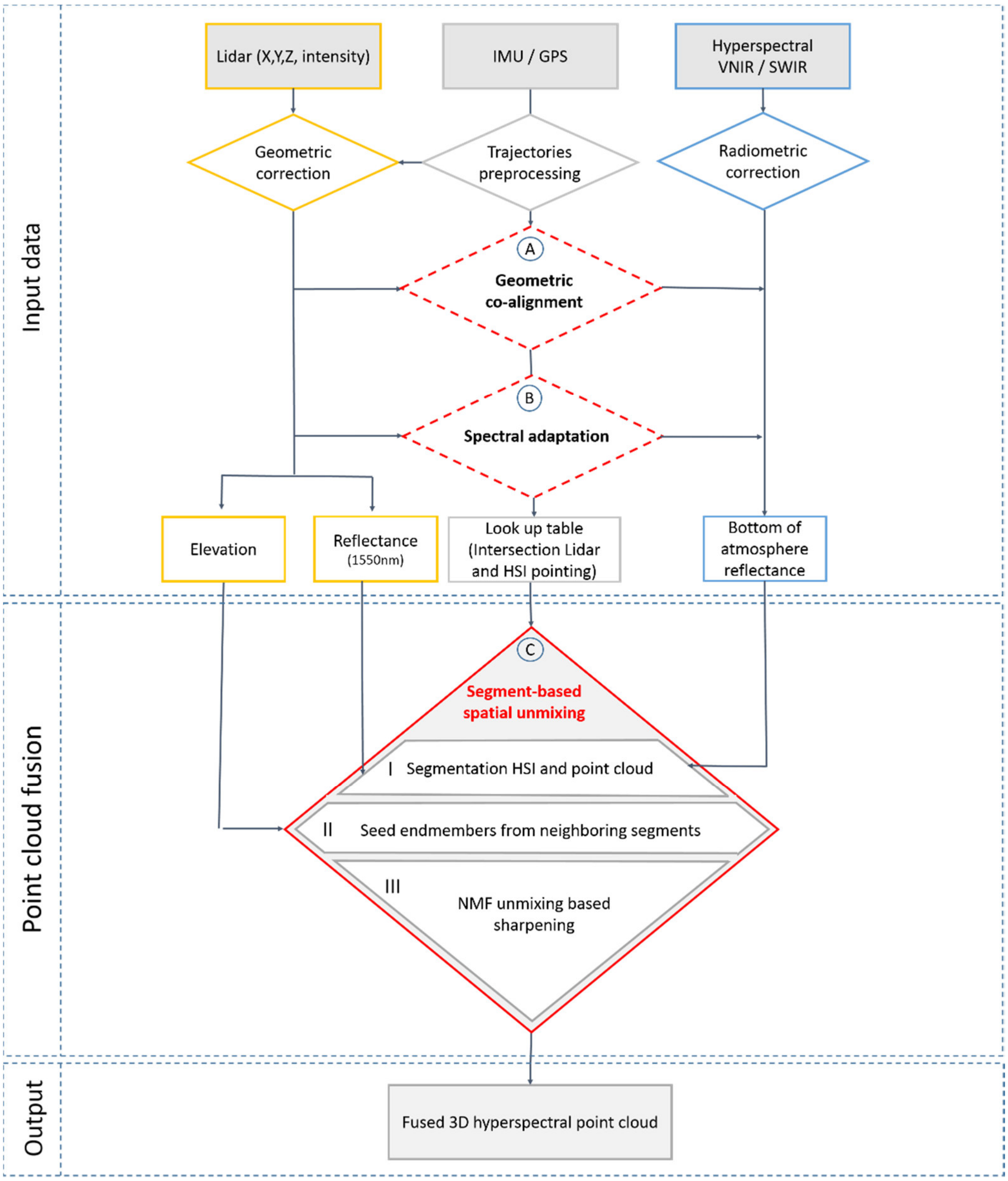

Fig. 2. Overview of the hyperspectral point cloud (HSPC) generation workflow. Data products are represented by rectangles, processing steps are represented by rhomboids, ALS pre-processing steps are indicated by yellow outlines, HSI data-related steps are indicated by blue outlines, preprocessing steps relevant for both datasets are outlined in gray, and red outlines are used for the major fusion steps.

3.1.1 Input data generation and preprocessing

To generate the HSPC, simultaneous ALS (RIEGEL; LMS-Q560) and HSI (Neo HySpex; VNIR-1600 and SWIR-320m-e) data were acquired over a heterogeneous sub-urban area. The resulting native ground sampling resolution of about 1.4 m for the HSI sensors and the point density of about 5 points/m² had to be aligned spatially and spectrally. Both sensors are co-aligned geometrically (Fig. 2 (A)) based on their respective intensity information with subpixel precision. The used approach is described in detail in Brell et al., (2016). Alternative approaches that deliver a precise subpixel co-registration of both sensors are equally adequate. Additionally spectral adaptation (Fig. 2 (B)) of both sensor responses is also a prerequisite of the fusion. It includes 3 pre-processing steps. First, an ALS point cloud filtering has to be performed. The goal is to include only the first returns, which represent the surface measured by the HSI and thus can be connected to the HSI signature. Both solar and lidar radiation penetrate vegetation structures. This nonlinearities inside vegetation are not considered. Therefore, higher-order returns inside vegetation cover will not be included (Brell et al., 2017). The assumption that, i.e. trees are well defined objects are a necessary simplification in processing. Second, a radiometric calibration of the ALS intensity data is performed which results in ALS bottom-of-atmosphere reflectance. Third, the atmospheric correction of the HSI data into bottom-of-atmosphere reflectance (Fig. 3 (C)) (Guanter et al., 2009) is implemented. Here, the complete spectral adaptation procedure is realized based on radiometric cross-calibration between the two sensor responses introduced by Brell et al. (2017). The cross-calibration approach used here has the advantage that it exploits the active sensor intensity information of the ALS sensor to eliminate object shadows, illumination effects, and anisotropic effects in the HSI data (Brell et al., 2017). During the preprocessing, a look-up table (Fig. 3 (D)) is prepared, which allocates the intersection of every single HSI pointing with the ALS point cloud by ray tracing.

3.1.2 Hyperspectral point cloud (HSPC) fusion

To establish the HSPC, we focus on the preservation of the spectral content of the HSI data by considering the spectral and spatial neighborhood of the high spatial resolution point cloud. The fused HSPC itself is realized with segment-based spatial unmixing (SSA) (Fig. 2 (C)). The presented spatial resolution enhancement is based on the spectral unmixing of HSI data using non-negative matrix factorization (NMF) (Fig. 3 (II-IIII) (3.1.2.2).

SSA is subdivided into three major processing steps (Fig. 3):

I. Segmentation-based endmember selection
II. Spatial unmixing based on non-negative matrix factorization

III. Generation of output matrix

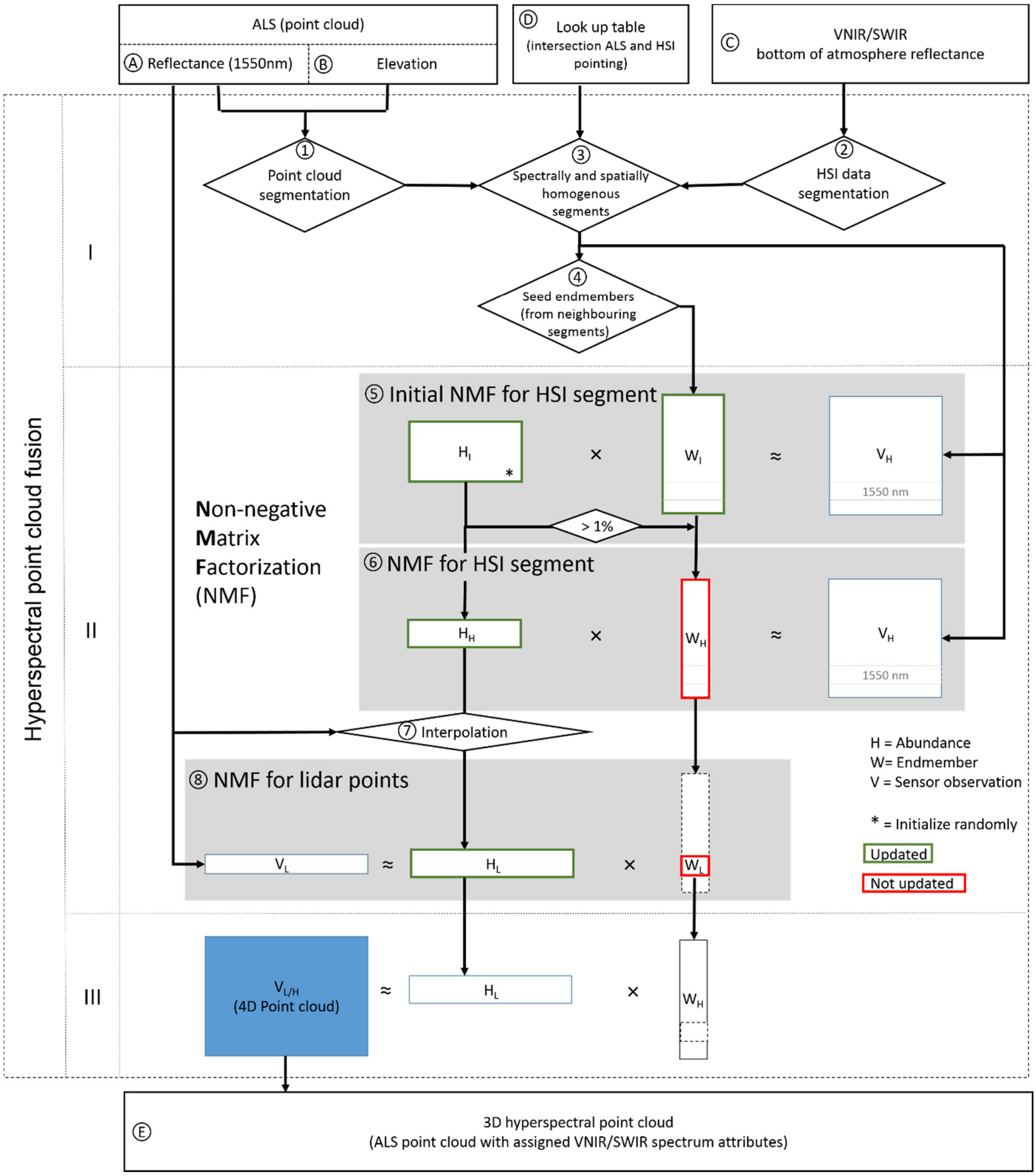

Fig. 3. Detailed workflow of the segment-based spatial unmixing. Input and output data products are represented as rectangles (A-E), and processing modules are represented by rhomboids (1-4). Gray shading highlights the non-negative matrix factorization (NMF) procedures. The involved matrices (W = endmembers, H = abundances, V_H = Hyperspectral data (low spatial resolution), V_L = Lidar data (high spatial resolution). The dimensions of the involved matrices are suggested by the extent of representing rectangles. The abundances are always updated during NMF (indicated by a green border). Endmembers are only updated during initial NMF (indicated by a red border).

3.1.2.1 Segmentation-based endmember selection

Preliminary over-segmentation of the data into segments performed before the unmixing-based sharpening (Fig. 4). This segmentation combines the spectral information from the HSI sensor with the original geometric and intensity information of the ALS data. The produced segments divide the data into spectrally and spatially homogeneous and inhomogeneous regions. Various features computed separately for HSI and ALS data are aggregated on the HSI pointing scale to indicate the variability as a fusion criterion. An eight-dimensional feature space is generated based on the first five principal components (representing 94.5 % of the spectral variation of the processed example point cloud) and three features extracted from the point cloud (ALS reflectance, local height, and normal vector). The three point cloud features are aggregated at the HSI pixel scale (Fig. 4 (3)) by calculating the variation of the features inside an HSI pointing. An alternative segmentation approach or easier accessible features are possible as long as the results can be understood as general homogeneity criterion, which indicates the spectral and spatial complexity inside an HSI pixel. We further discuss the point-cloud feature derivation in section 5.

The generated feature space is partitioned into clusters by a k-means algorithm. The number of potential clusters is not explicit; it depends on the heterogeneity of the scene and should be chosen to be sufficiently high to guarantee over-segmentation. For the example data set, 60 clusters have been shown to be adequate. Over-segmentation is intended to keep the spectral and spatial variance and the potential numbers of endmembers small inside a segment. The clustered pixels are regionally labeled to give spatially neighboring pixels the same segment association. To determine potential endmembers within a segment, a pixel is selected by extracting geometric and spectral segment features. A potential seed endmember should be as far as possible from the segment border. In addition, the ALS intensity, elevation and facet normal variations should be as small as possible within a pixel. A ranking of the pixels within every segment is realized, and the pixels with the smallest variations and distance from the morphological segment center are marked as potential endmember candidates (Fig. 4 (4), pixels numbered 0-3). These endmembers represent the spectral and spatial complexity of a certain segment.

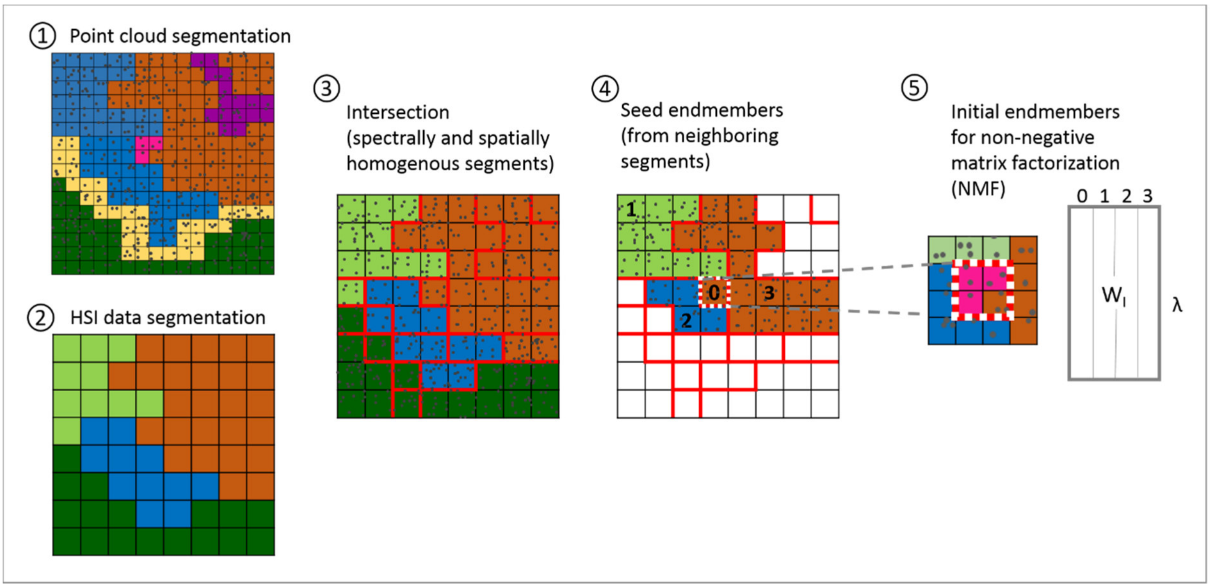

Fig. 4. Scheme of segmentation-based endmember reduction. (1) Point cloud is indicated by irregular points, and its segmentation is indicated by rasterized colored patches. (2) HSI data segmentation. (3) Red bordered patches represent the spectrally and spatially homogenous segments, which result from the intersection of (1) and (2). (4) Segment of interest (dashed outline) with relevant neighboring segments (colored red-bordered patches). Numbers indicate the HSI spectra used as seed endmembers for unmixing the segment of interest. (5) Subset representing the segment of interest (dashed outline) with relevant neighbors at point cloud scale and the resulting initial endmember matrix.

3.1.2.2 Spatial unmixing based on nonnegative matrix factorization (NMF))

The presented NMF unmixing-based ALS intensity sharpening is adopted from already established methods based on NMF unmixing for hyper- and multi-spectral as well as panchromatic data fusion (Loncan et al., 2015; Yokoya et al., 2012). The technique relies on the assumption that the spectrum represented by an HSI pixel is based on a linear combination of several endmembers and can thus be factorized by two non-negative matrices W and H (Fig. 3 (5)). The matrix W accounts for the endmembers and H for relative abundances. Since the potential endmembers W are known we can approximate their relative abundances based on minimization. In the following, we describe the use of NMF for the spatial unmixing in detail. The NMF unmixing is carried out for each segment, including the potential endmember candidates of the adjacent segments. In the first step (Fig. 3 (5)), the initial endmember candidates (W_I) for a certain segment are reduced by NMF. The abundance matrix (H_I) is initialized randomly, and the minimization performed with the multiplicative update rule (Lee and Seung, 2001). The initial endmember candidates (W_I) are also updated by the NMF. Only the most important endmembers (W_H) whose abundances (H_I) have a fractional amount > 0.1 % are used for the unmixing of a certain segment in the second step (Fig. 3 (6)). These endmembers (W_H) are not updated in contrast to the randomly initialized HSI abundances (H_H). These abundances (H_H) are interpolated spatially to the distribution of the irregular ALS point cloud using bilinear interpolation (Fig. 3 (7)). The resulting interpolated abundances (H_L) are initially used, while W_L is not updated by the multiplicative update rule during minimization (Fig. 3 (8)).

3.1.3 Hyperspectral point cloud (HSPC) output

The generated output matrix bundled with the X, Y, Z information of the ALS point cloud represents the HSPC (X, Y, Z and spectra).

3.2 Object-based information extraction method

We apply a data assessment approach specifically designed for the evaluation of the spectral and structural information content of the generated HSPC. Standard classification and segmentation procedures are used to examine the spectral and structural information content of the generated HSPC at the object scale. In a first step, the spectral information content of every HSPC point is classified with a supervised classification procedure. We implement a support vector machine (SVM) algorithm (Chang and Lin, 2011), because it has been shown to be powerful in classifying high-dimensional spectral data (Melgani and Bruzzone, 2004). Next, we split the HSPC based on spectral class affiliation into several single point clouds. These point clouds represent the various spectral sub-classes and are then segmented individually based on their structural information content by a basic 3D point cloud segmentation technique. The implemented structural segmentation procedure (Cluster-All algorithm, Douillard et al., 2011) is a voxel-based connected component labeling. Instead of using the bare ground surface filtering as initial separation between freestanding point cloud objects (Douillard et al., 2011), we have already pre-segmented the point cloud beforehand by splitting the HSPC based on spectral class affiliation.

4 Results

4.1 Hyperspectral point cloud (HSPC)

The generated HSPC is shown in Fig. 5. To illustrate the combined spectral and structural properties and the overall character, the HSPC is shown from three different points of view and with different color composites (A: RGB (red, green, blue); B: CIR (color infrared) and C: MS ALS).

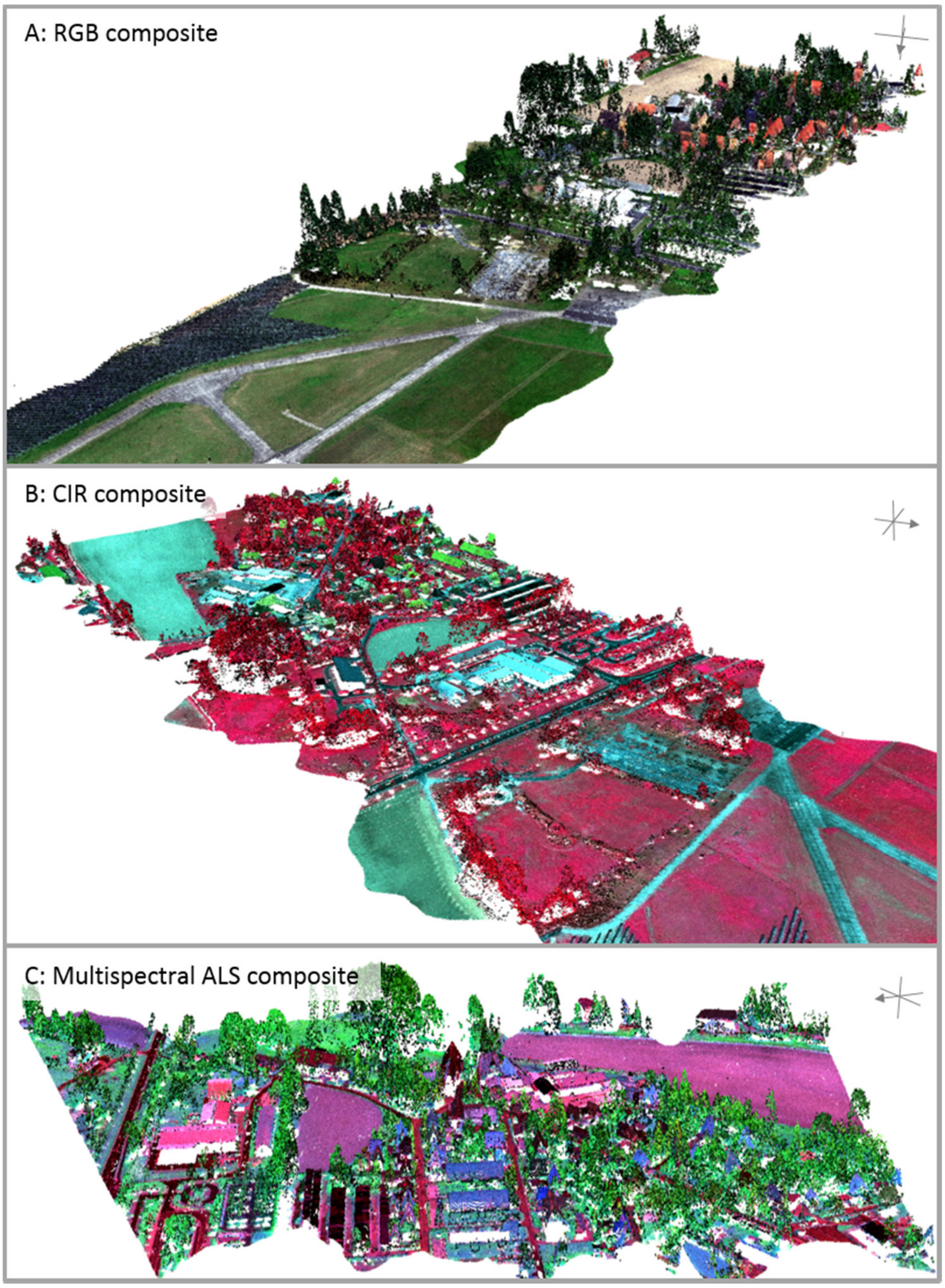

Fig. 5: Different perspective views and color composites of the hyperspectral point cloud. (A) RGB composite (R = 640 nm, G = 549 nm, B = 469 nm), (B) CIR (R = 851 nm, G = 640 nm, B = 549 nm), and (C) example of a MS ALS composite (R = 532 nm, G = 1069 nm, B = 1550 nm).

The initial visual investigation of the point cloud shows that the assignment of the spectra distinctively reflects the morphological object borders. This indicates a successful assignment of a HSI spectrum to every first return ALS point.

We perform a detailed investigation of the HSPC in the following two chapters. The performance of the SSA and the valid transfer of the hyperspectral information acquired by the HSI sensor to the high-spatial resolution of the ALS point cloud are verified spatially (4.1.1) and spectrally (4.1.2). Since there are no extensive ground truth data available which meet the high spatial and spectral resolution of the resulting HSPC, an absolute accuracy assessment is not possible. Therefore, the HSPC can only be evaluated relative to its original data or relative to a conventional draping method. For evaluation purposes we generated a more traditionally fused hyperspectral point cloud by matching the nearest neighbor pixel of the co-registered HSI image to every XYZ lidar point (nearest neighbor assignment (NNA)). This NNA point cloud represents the standard method for draping HSI information to a point cloud. For direct comparison it is important that the NNA point cloud has the same spatial metric as the HSPC. However, the spectral information is draped by NNA in HSI sampling resolution. We explain this relative evaluation in the following chapters in detail.

4.1.1 Enhancement of spatial content

The spatial enhancement accompanied by the assignment of the spectral information to the ALS point cloud is validated by the visual inspection of the gridded RGB HSPC information (Fig. 6). The visual comparison against the original HSI data indicates that the spatial enhancement is also realized for the non-overlapping true color RGB wavelength. In general, the blurred impression of the HSI image is replaced by the spatially high contrasting ALS characteristic. Spatial patterns, which are slightly indicated but not traceable in the HSI image, are carved out in the gridded RGB image Fig. 6 B (blue outline), representing the fused point cloud. In particular, single trees and sidewalks (Fig. 6 (1 B and 5 B)), road markings (Fig. 6 (2 B)) and thin tar joints between concrete slabs (Fig. 6 (3 B)) show that the overall object delineation and selectivity have been significantly improved for all subsets. The absolute difference images (Fig. 6 C 1-5) indicates that the object borders introduce the greatest differences, whereas the unmixing-based fusion only slightly influences homogenous areas. All these findings suggest that the high spatial information of the ALS data is implemented correctly in the spectral information. Apart from that, the NNA approach which can be seen as a more traditionally method to drape spatially course HSI data to a point cloud, does not improve the spatial content and delivers the same blurred impression as the original HSI data; therefore, it is not shown separately.

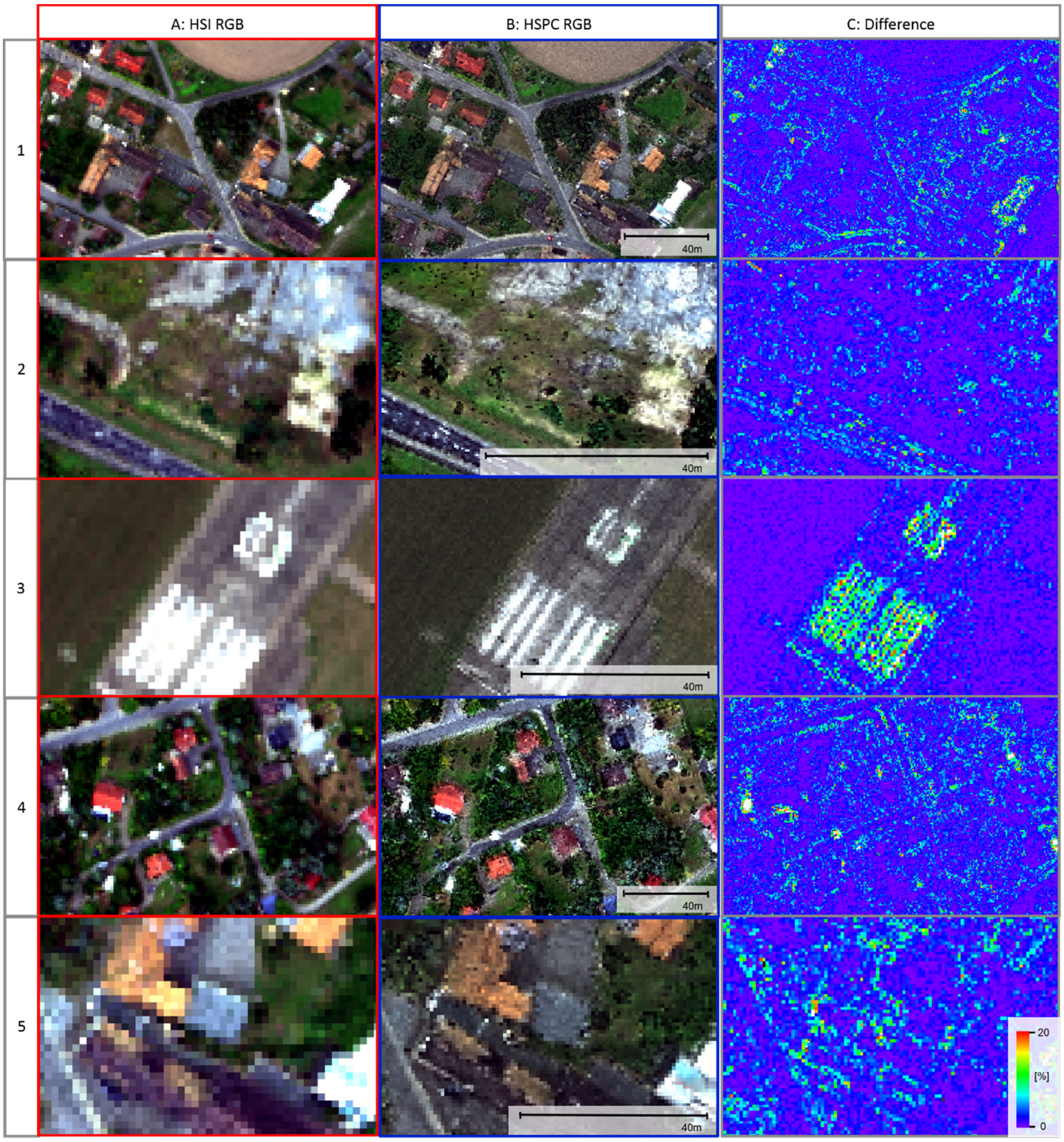

Fig. 6: Spatial comparison of the fusion procedure based on four (1-5) different gridded RGB color composite subsets (R = 640 nm, G = 549 nm, and B = 469 nm; images are displayed with 1 % linear global stretch). (A 1-5) Geo-corrected HSI reflectance images resampled to original ground sampling distance of 1.4 m. (B 1-5) Geo-corrected hyperspectral point cloud gridded to a resolution of 0.5 m. (C 1-5) Absolute difference between HSI reflectance images subsampled to 0.5 m by cubic convolution and (B) for 549 nm wavelength.

4.1.2 Preservation of spectral content

The presented approach is designed to preserve the spectral content of the hyperspectral data. For validation, the spectral root-mean-square error (RMSE) between the original HSI spectra and the corresponding reverse degraded SSA spectra is calculated. The spatial reverse degradation of high spatial resolution HSPC to native HSI ground sampling distance is realized by weighting the hyperspectral points, which intersect with an HSI cone, with its point spread function (PSF). The image of the RMSE (Fig. 7 (A)) indicates that the preservation of the spectral content is poorer for spatially and spectrally heterogeneous areas. These differences are expected because of small geometric co-registration problems and increased non-linear mixing conditions. However, the histogram shows that in these areas, the RMSE does not exceed 2 % reflectance. The mean RMSE is approximately 1.25 %, and the standard deviation of 0.33 % is minimal.

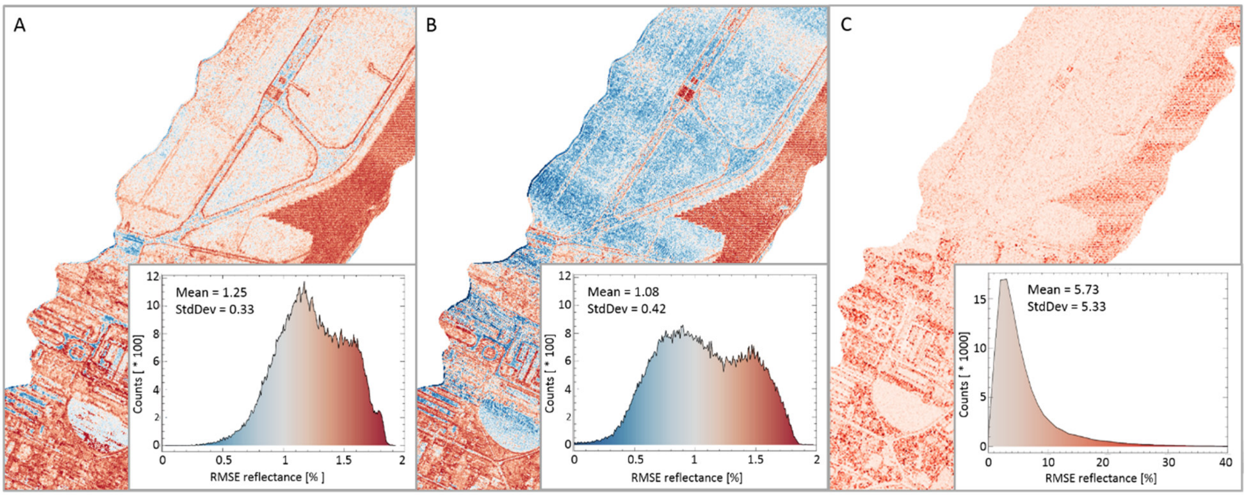

Fig. 7: Spectral deformation represented by RMSE images and histograms. (A) Spectral RMSE calculated between original HSI spectra and the segmentation-based spatial unmixing (SSA) point cloud which was spatially resampled to the spatial resolution of the original HSI data, (B) spectral RMSE calculated between original HSI spectra and the natural neighbor assignment (NNA) point cloud which was spatially resampled to the spatial resolution of the original HSI data, and (C) spectral RMSE calculated between SSA and the NNA assignment.

For a comparison, the RMSE between the spectra of original HSI data and spatially adopted spectra based on NNA assignment are shown in Fig. 7 (B). The spectral preservation of both assignment methods (SSA and NNA) is in agreement. Both approaches result in spectral RMSEs that are smaller than 2 % reflectance. A slight shift toward higher RMSEs is ascertainable for the unmixing-based spectra assignment Fig. 7 (A). Direct comparison between the spectral assignment based on the nearest neighbor and the presented SSA approach is realized by calculating the spectral RMSE between the point clouds (Fig. 7 (C)). The higher mean RMSE (5.73 %) compared to the mean RMSE between original HSI data and SSA (Fig. 7 (A)) and mean RMSE between original HSI data and NNA (Fig. 7 (B)) indicates that the spectral variation inside an HSI beam is well described. The increase in spatially induced spectral variance and thus the spatial enhancement of the SSA approach is confirmed. The subsets of Fig. 8 shows the RMSE differences between the two point clouds. Not surprisingly, the patterns outlining the objects indicate that the nearest neighbor technique is not feasible to model the morphological shape of a certain object in a spectrally consistent manner. However, the areas where no spatially induced spectral variance occurs, indicate that the spatial HSI resolution is adequate and that no improvement is achieved through using a higher-spatial resolution ALS point density. This scale-dependent issue is discussed in more detail in chapter 5.1.

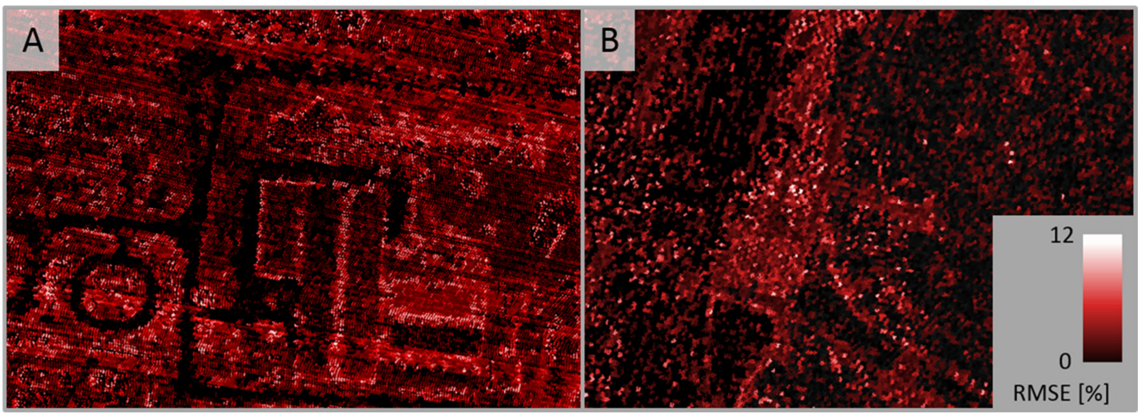

Fig. 8: Subsets of point cloud comparison. RMSE between NNA and segment-based unmixing (SSA) spectrum assignment for (A) an urban area and (B) a runway.

4.2 Object-based information extraction

Many application in ecology and geography require object identification and existing analysis method rely on object-based assessments for the derivation of biochemical, biophysical, and earth surface object parameters. The main advantage of the fused HSPC compared to the separated entities is the combination of spectral and structural characteristics, which are represented at the same spatial scale as the point cloud. To obtain a realistic and application independent understanding of the quality and advantages of the proposed HSPC generation, we evaluate the synergistic benefits of structural and spectral information in a single entity for biophysical and earth surface parameter estimation in this section.

4.2.1 Spectral point cloud classification

A classification comparison is performed to assess the spectral information content of the HSPC and to illustrate the spectral potential of the developed fusion approach. The result of classifying the generated HSPC (spectral + elevation properties) into seven common object classes is shown in Fig. 9 (A)

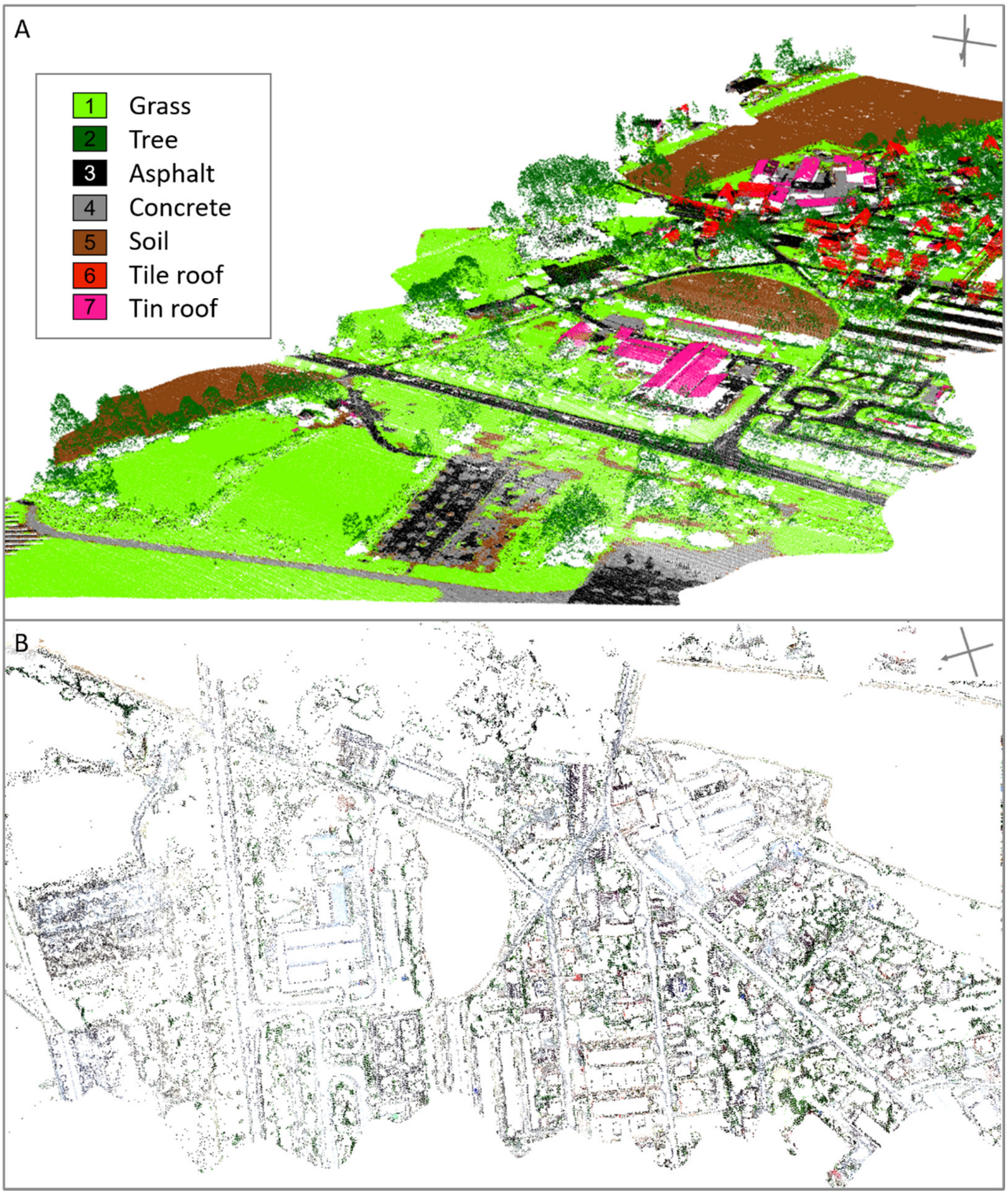

Fig. 9 (A) Perspective view of the HSPC classification results (Table 1 (1); classification is performed with a supervised support vector machine classification of spectral and elevation properties). (B) Map view showing classification differences between HSPC and NNA point cloud (see Table 1 (1 & 2)).

The assignment of spectra to a single first-return point results in a precise classification of a single point due to its high information content (X, Y, Z, spectra). From 123.741 reference HSPC points used for validation, 121.825 have been classified correctly. This result indicates an overall classification accuracy of 98.45 % with a kappa coefficient of 0.96. Elevated objects such as trees and roofs can be separated more easily due to the consideration of their object height and 3D structure during the classification procedure. In addition, ground or near-ground objects are classified with high accuracy. To put this result into context, a classification comparison has been carried out. The original ALS and HSI data, traditionally fused raster data (stacked hyperspectral image + digital surface model) and the point cloud assigned by NNA were also classified (Table 1).The result of the HSPC classification shows only a small advantage over the merged raster data and the NNA point cloud (Table 1). However, the available ground truth data used for validation does not reflect the high spatial and spectral contrast present in the HSPC (see 4.1.1 and 4.1.2). Because of this constraint, the expected higher spectral separability of the HSPC appears to be low-to-moderate in the classification comparison. Ground truth with spatial and spectral resolution of the HSPC would emphasize classification differences more strongly.

Table 1 Classification accuracies of HSPC, NNA, fused grid data and source data sets

Fused point clouds	**Overall classification accuracy [%]**	**Kappa coefficient**
1. Hyperspectral point cloud (HSPC) (HSI + Elevation; 400-2500 nm; 267 channels)	98.45	0.96
2. Hyperspectral point cloud (NNA) (HSI + Elevation; 400-2500 nm; 267 channels)	98.07	0.95
Fused grid data	**Overall classification accuracy [%]**	**Kappa coefficient**
3. Hyperspectral image + Digital surface model (HSI; 400-2500 nm; 267 channels + elevation)	96.88	0.95
Source data sets	**Overall classification accuracy [%]**	**Kappa coefficient**
4. Original hyperspectral image (HSI; 400-2500 nm; 267 channels)	80.69	0.69
5. Original airborne laser scanner point cloud (ALS reflectance + elevation)	60.46	0.22

For, the HSPC significant amounts of concrete were falsely assigned to asphalt and soil (omission error Table 2). Also, asphalt was falsely assigned to concrete. Furthermore, soil and asphalt was misclassified as tile roof.

Table 2 Accuracy (Acc), commission (Com) and omission (Om) errors in percent [%] for the different point cloud classifications. Gray labeled cells indicate strikingly significant errors.

Class	1 HSPC (HSI + Elevation)			2 NNA (HSI + Elevation)			3 Grid data (HSI + Elevation)		
	Acc	Com	Om	Acc	Com	Om	Acc	Com	Om
Grass	99.91	0.32	0.09	99.93	1.18	0.07	99.17	0.85	0.83
Soil	99.51	6.38	0.49	99.19	4.79	0.81	99.63	4.84	0.37
Tree	96.30	0.72	3.70	77.90	0.74	22.10	79.71	16.74	20.29
Tile roof	93.38	6.28	6.62	97.01	7.88	2.99	96.44	5.36	3.56
Concrete	80.85	0.96	19.15	85.63	3.19	14.37	85.38	3.20	14.62
Tin roof	99.53	0.39	0.47	99.76	0.55	0.24	71.28	0.00	28.72
Asphalt	92.09	12.23	7.91	85.48	4.42	14.52	99.17	0.85	0.83

Fig. 9 (B) shows the falsely classified points from the NNA point cloud as compared to the HSPC classification. The visual inspection of Fig. 9 (B), confirms that the differences occur at the surface and object borders for concrete, soil, asphalt, tin roofs, and near ground trees, such as hedges. These areas are not sufficiently covered by the ground truth data. Despite an oversimplification due to generalized classes, the HSPC investigation indicates that the assigned hyperspectral information leads to a more accurate object discrimination and thus improves the overall point cloud filtering and real object classification capabilities. The reduced spectral information is also sufficient to classify a single point with high probability, but the HSPC outperforms them. The overall preservation of high spectral and spatial 3D elevation information indicates that more diverse classes without implicit oversimplification are feasible; however, the direct observation and thus to assess their classification accuracy entirely is more challenging.

4.2.2 Hierarchical point cloud segmentation

Adequate point cloud segmentation is an essential step for the modeling and capturing of real-world objects. We perform a segmentation to assess 3D object information. We demonstrate the combined spectral and structural potential in object-based classification of the HSPC (Fig. 10 A-D).

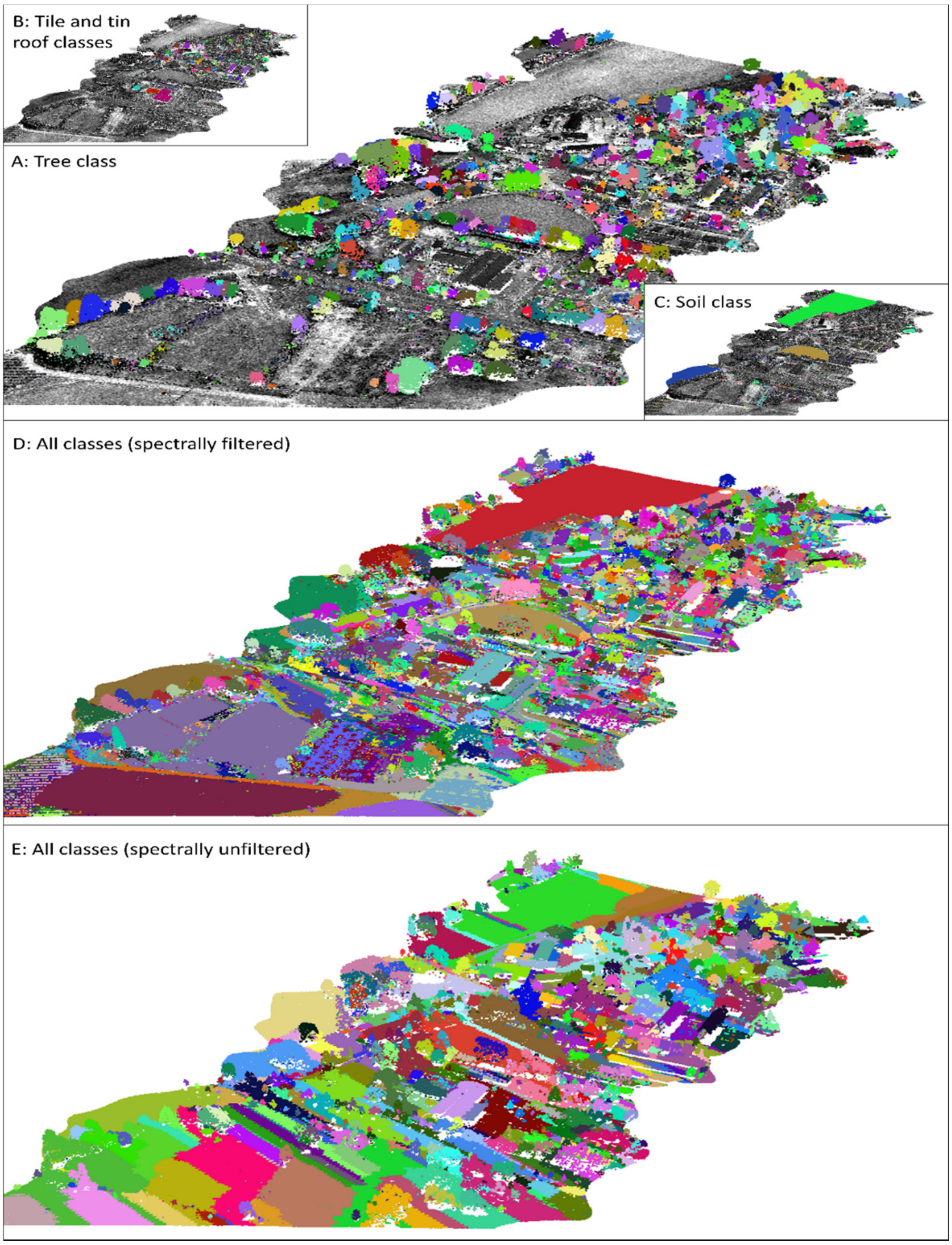

Fig. 10 Perspective view of the labeled object segments; (A) – (C) Hierarchical segmentation of previous spectrally filtered point clouds (A) for the tree class, (B) for tile and tin roof classes, (C) for the soil class, (D) for all classes and (E) segment labeling of a spectrally unfiltered HSI point cloud.

Due to the previous complexity reduction of the point cloud based on high-accuracy spectral classification, a simple segmentation method is sufficient to subdivide and label the point cloud into meaningful surface objects (Fig. 10 A-C). The automatic detection of individual trees (Fig. 10 A), roofs (Fig. 10 B) and soil patches (Fig. 10 C) is shown not only for free-standing objects but also for overlapping and densely distributed objects (Fig. 10 D). As expected, without preceding spectral filtering, the simple point cloud segmentation approach cannot adequately handle the complexity (Fig. 10 E). Neighboring spectrally heterogeneous surfaces with structural homogeneity are segmented into mindless patches. Advanced segmentation and classification approaches are feasible to handle this complexity to a certain degree. However, the hierarchical point cloud segmentation demonstrates that an accurate preceding or integrated spectral point cloud filtering supports the 3D object level access.

4.2.3 Derivation of object-based parameters

The object-based point cloud measurement and calculation of certain parameters, for example, the local variance of parameters, ground projection area and volume of certain objects, are obligatory for a great number of environmental applications. To demonstrate the potential of the HSPC and an object-based information extraction, we show the difference and dependencies of object parameter estimations from two different point clouds (HSCP and NNA, Table 3). Table 3 gives an impression of the sensitivity regarding the spectral assignment method for parameter estimation as well as the relevance of the developed fusion approach for applications.

Table 3: Statistical comparison of object parameter differences between mean object parameters derived from the hyperspectral point cloud (HSPC) and natural neighbor-based assignment (NNA); negative values indicate classes where the mean derived object parameter is greater for NNA assignment, green marked cells indicate expected values, and orange cells indicate selected values for discussion.

	Difference (HSCP – NNA)						
	Total number of segments	Spectral object variability [%]	Structural variability [m]	Max object height [m]	Mean object height [m]	Projected object area [m²]	Object volume [m³]
Grass	-468	-266.53	-0.465	-1.98	-0.56	-198.51	-11.78
Trees	-285	127.47	0.47	2.69	0.94	113.21	2.5
Asphalt	261	-89.08	0.22	0.61	-0.13	115.07	1.09
Concrete	-237	-278.08	-0.1	-0.49	-0.13	61.3	-1.4
Soil	-695	-98.18	0.09	0.67	0.3	245.29	0.02
Tile roof	-360	-40.06	-0.06	1.82	1.81	8.17	0.77
Tin roof	-100	-189.27	0.07	1.8	1.4	27.92	1.18

The differences between the mean derived object parameters for the respective classes do not show a clear tendency. The reasons are complex and depend on the spatial and spectral homogeneity of a class and its objects, its surroundings and spatial overlaps. Therefore, the individual interpretation is difficult and, to a certain point, speculative. However, some notable values are discussed: The difference between the total amounts of respective segmented objects shows that fewer objects of a class are generated and that the mean spectral object variability is predominantly reduced for the HSPC data basis. The mean projected area of an object is also increased. This circumstance indicates that the spectra are not assigned accurately to the object shape by NNA. The conducted segmentation leads to smaller patches around the objects and overall fragmentation. Asphalt stands out because the number of objects and the measured projected area are increased which was also observed in the classification results. In addition, the mean projected grass area indicates an effective reduction probably at the expense of soil. The overall spectral and structural variability for trees is increasing for the HSPC. Trees consist of leaves and branches, and thus, they are inherently spectral and structural heterogeneous objects. It seems that HSPC assignment reflects this trait less discretized. The increased parameters (tree max, mean object heights and the projected object area) as well as the relatively stable object volume parameter support this interpretation. In any case, the overall consideration indicates the sensitivity of the parameter estimations to the spectra assignment. It can be concluded that object parameter derivation based on combined HSI and ALS data is significantly sensitive to an appropriate data fusion. This circumstance is highly relevant for environmental applications. In general, these standard parameters and more advanced empirically modeled parameters are easily derivable from the fused 3D HSPC. Studying the spectral and spatial variability of these parameters can be easily realized with the HSPC and enhances the differentiation within object classes. This approach provides the opportunity to differentiate between types and statuses of objects at the point cloud level.

5 **Discussion**

The generation of HSPCs is an emerging method with currently only very limited existing research. The fusion approach proposed in this work adds to the growing body of literature and the manuscript attempts to provide relevant background information. The opportunities and limitations for applications resulting from the HSPC generation (chapter 3.1) and the performed OBI (chapter 3.2) are discussed in detail below.

5.1 Hyperspectral point cloud (HSPC) generation approach

The presented ALS and HSI data fusion relies on segmentation-based spatial unmixing. The resulting HSPC indicates that the spectral assignment to an irregular point cloud is a clear spatial enhancement. It is shown that the developed approach is capable of assigning spectra to the spatially irregular ALS point cloud. Furthermore, simple NNA is not sufficient for precise spectral assignment. Thereby, the following three inherent fusion challenges have been solved successfully:

(1) The narrow wavelength overlap compared to the wide HSI spectral range of the two sensors;
(2) the low-intensity contrast between certain objects in the overlapping wavelength domain; and
(3) the irregular spatial distribution of the ALS point cloud.

Additionally, the results show that the generated HSPC improves classification and segmentation accuracies for heterogeneous environments by appropriate fusion of the data entities. Compared to pixel-level discretized data, the HSPC reproduces extreme local spectral and structural variations. Thus, the fused HSPC enables new opportunities for point cloud filtering and object-based parameter estimation. However, three prerequisites must be fulfilled to gain such accurate results with the presented approach. First, ALS and HSI data must be co-registered precisely. Second, the ALS point cloud should only represent first returns which can be connected to the HSI signature. Therefore, higher order returns inside vegetation, which have no assignable contribution to the spectral signature in the HSI, cannot be assigned with a proper spectrum. Third, the ALS data have to be radiometrically calibrated and the HSI data has to be atmospherically corrected. Due to the performed preprocessing (see3.1.1), the represented fusion approach is capable of handling geometric co-registration issues (Brell et al., 2016), sensor cross-calibration and thus passive illumination drawbacks (Brell et al., 2017) to support the elimination of spectral and spatial resolution incompatibilities. However, alternative standard approaches are sufficient for the fusion.

Despite the slightly larger deformation of the spectral information compared to the original HSI data (Fig. 7 (A and B)), the classification and segmentation performance results in proper and clear delineation of the relevant surface objects. It is beneficial for the generation of the HSPC to optimize the HSI endmember set on a per-segment basis. The per-segment processing is computationally efficient. Reducing the number of iterations and of potentially involved endmembers reduces the number of matrix calculations compared to pixel-oriented approaches. Furthermore, restrictions that are caused by the insufficient intensity contrast among all relevant land-cover classes in the 1550 nm domain can be overcome by the SSA, and the wrong mixture results caused by poor endmember selection are prevented with the preceding segmentation. The approach is based on the assumption that endmember pixels are located in the adjacent and respective segments. Thus, building the segments is a sensitive key step in the fusion procedure. The intended tendency to over-segmentation ensures that the segments are not underrepresented by the optimized endmember set. Calculating the point cloud feature variability on the HSI pixel scale is efficient to capture the spectral heterogeneity inside a pixel and thus inside the segment. The results indicated that the segmentation is essential but the type of segmentation is not crucial. Alternative point cloud features for the segmentation are possible as long as the overall focus is retained. The over-segmentation should differentiate the data into segments representing spectrally and spatially homogeneous regions and inhomogeneous regions. For the unmixing procedure itself, NMF was used because it is easy to implement and to adopt despite remarkable performance (Loncan et al., 2015; Yokoya et al., 2012).

However, the overall quality and operability of the fusion approach are dependent on the proportion of HSI resolution to ALS point density. Additionally, the spatial and spectral surface heterogeneity itself and the spatial distribution of the ALS points inside one HSI pixel have an effect on the resulting data quality. Ultimately, the optimal proportion depends on the application scale. For this study, 3-4 points per HSI pixel seem to be a minimum for an improvement of the more heterogeneous parts (trees, urban structures). However, for the more homogeneous parts (streets, runway), where the point density is generally higher, also small spatial features such as lane marking or concrete joins can be sharpened. The point density for the runway area and the roads is up to 10-20 points per square meter. A low surface heterogeneity but high point density leads to a higher spatial and spectral accuracy and vice versa. In principle, one can say that the higher the ALS point density is compared to the native HSI resolution, the better the fusion quality. Due to the overall scale-dependency, we avoid a set definition of the proportion between the point cloud density and the spatial resolution. The application determines the scale of the point-cloud data collection and point-cloud analysis.

5.2 Application perspectives

The developed fusion approach is holistic in order to support a broad range of environmental, urban local to regional applications with state-of-the-art spectral and spatial remote sensing data. The demonstrated improved object-based information extraction introduced by the fusion is an outstanding advantage for a great number of environmental and urban applications. Especially the reduction of the intra-class variability and the enhancement of the inter-class separability (see 4.2.1) significantly improves the overall information content. Additionally, due to the assigned active ALS measurement characteristic to the HSI data which reduces illumination and shadowing issues (Brell et al., 2017), even advantages reserved for active lidar measurements (Dai et al., 2018; Zou et al., 2016; Suomalainen et al., 2011) can be reproduced and implemented. Compared to a surface description based on the combination of photogrammetric 3D surface models and HSI spectral information (Aasen et al., 2015; Nevalainen et al., 2017; Oliveira et al., 2019), the HSPC provides full ALS inherent structural and spatial quality characteristics (including multiple returns within the vegetation). In addition, such combinations have so far only been limited to the VNIR spectral range and consistent illumination correction in a physical manner is an unsolved issue.

The demonstrated HSPC inherent capability of spectral point cloud filtering reduces the structural complexity and contrasts the dissimilarities (4.2.2). Compared to the complex complete point cloud, the resulting spectrally homogeneous subclasses can be segmented structurally more easily also with very simple segmentation approaches. More sophisticated segmentation approaches, which need a priori knowledge to consider certain object shapes and structures are not mandatory anymore. Additionally, structurally similar but spectrally heterogeneous surface patterns can be differentiated or recognized as separated objects with the support of spectral information.

In general, it is preferable to support applications with maximum flexibility regarding the scale of measurement. The HSPC has the potential to accomplish the spatial and spectral scalability to meet customized demands to the highest measured scale. Due to the Airborne technology of the sensors the HSPC is especially suited for applications that serve a regional to local scale level. With increasing miniaturization of the sensors and the professionalization of the UAVs, it will be possible to combine the properties of both sensors on these platforms as well (Sankey et al., 2017). It is shown (see 4.2.3) that the generated HSPC is an adequate and powerful data basis and especially biophysical, biochemical, and earth surface parameter estimation can profit from the scalable point cloud metric. In particular, the scalable combination of spectral and structural information on a point cloud level is beneficial for environmental parameter derivation for mixed land covers, where the point cloud metric is not inevitably the dominant attribute.

5.3 Opportunities and limitations

The potential of HSPCs is demonstrated by classifying (see 4.2.1) and segmenting (see 4.2.2) the generated point cloud and by showing object level parameter estimation for certain applications (see 4.2.3). Based on the evaluation of the generated HSPC, the following opportunities can be highlighted:

1. The data fusing at the point cloud level enhances the potentially available analyzing scale, and thus expands and combines the scope of both technologies. The information

content of the point cloud can be adjusted and application-oriented to special issues or scales.

2. Accurate spectral point cloud filtering of certain land-cover classes can be utilized at the individual point level based on hyperspectral methods (classification, dimension reduction techniques).
3. The opportunity to combine HSI classification and point cloud segmentation capabilities results in overall improvement of object recognition robustness.
4. Improved and intuitive object level parameter estimation based on spectral and three-dimensional geometric information is enabled.

The following limitations for applications can be mentioned:

1. The overall quality of the data fusion is sensitive to the proportion between point cloud density and spatial resolution of HSI data.
2. ALS points reflected inside vegetation bodies (higher-order returns) that are not represented in hyperspectral data cannot be provided with adequate spectra.
3. The resulting HSPC is subsect to an increasing complexity of required methods considering acquisition, data access, storage, fusing and analyzing strategies compared to raster approaches.

6 **Conclusion**

In this study, we have presented a comprehensive approach for fusing spectral and 3D data derived from a hyperspectral imaging system and airborne lidar system. The developed segmentation-based spatial unmixing is capable of assigning hyperspectral information to every first-pulse return of the high-spatial resolution airborne laser point cloud. The generated HSPC combines spectral and three-dimensional information content at the spatial scale of the point cloud in a single data entity. It thus represents the high spectral and spatial resolution and overcomes the discretization inherent to the respective sensor characteristics. The HSPC provides enhanced context, which can be easily accessed, filtered, and parameterized. We have demonstrated that the HSPC includes the capability of simultaneous spectral classification and 3D structural segmentation, which enhances object identification and information extraction. The combined hyperspectral classification and 3D structural segmentation capabilities improves the filtering and object parameter estimation as well as the object recognition. This fulfills a key requirement of various environmental and urban applications and opens up new opportunities for the object-based derivation of biophysical, biochemical, and earth surface parameters. As a final result, the generated HSPC delivers a consistent data stream with enhanced information content and has the potential to greatly improve the semantic labelling and modelling of real-world objects.

Acknowledgements

The Helmholtz Centre Potsdam - GFZ German Research Centre for Geosciences and the funding program “Zentrales Innovationsprogramm Mittelstand (ZIM)” founded by the Federal Ministry for Economic Affairs and Energy Germany (BMWi) have financed this research. In addition, to this financial support, the authors would like to thank MILAN Geoservice GmbH, for technical ALS sensor and flight campaign support. Finally, we would like to thank Dr. Sigrid Roessner for constructively streamlining the manuscript.

References

Aasen, H., Burkart, A., Bolten, A., Bareth, G., 2015. Generating 3D hyperspectral information with lightweight UAV snapshot cameras for vegetation monitoring: From camera calibration to quality assurance. ISPRS J. Photogramm. Remote Sens. 108, 245–259. https://doi.org/10.1016/j.isprsjprs.2015.08.002

Alonzo, M., Bookhagen, B., McFadden, J.P., Sun, A., Roberts, D.A., 2015. Mapping urban forest leaf area index with airborne lidar using penetration metrics and allometry. Remote Sens. Environ. 162, 141–153. https://doi.org/10.1016/j.rse.2015.02.025

Alonzo, M., Bookhagen, B., Roberts, D.A., 2014. Urban tree species mapping using hyperspectral and lidar data fusion. Remote Sens. Environ. 148, 70–83. https://doi.org/10.1016/j.rse.2014.03.018

Anderson, J.E., Plourde, L.C., Martin, M.E., Braswell, B.H., Smith, M.-L., Dubayah, R.O., Hofton, M.A., Blair, J.B., 2008. Integrating waveform lidar with hyperspectral imagery for inventory of a northern temperate forest. Remote Sens. Environ. 112, 1856–1870. https://doi.org/10.1016/j.rse.2007.09.009

Asner, G.P., Knapp, D.E., Kennedy-Bowdoin, T., Jones, M.O., Martin, R.E., Boardman, J., Field, C.B., 2007. Carnegie airborne observatory: in-flight fusion of hyperspectral imaging and waveform light detection and ranging for three-dimensional studies of ecosystems. J. Appl. Remote Sens. 1, 013536–013536.

Asner, G.P., Martin, R.E., Knapp, D.E., Tupayachi, R., Anderson, C.B., Sinca, F., Vaughn, N.R., Llactayo, W., 2017. Airborne laser-guided imaging spectroscopy to map forest trait diversity and guide conservation. Science 355, 385–389.

Bioucas-Dias, J.M., Plaza, A., Dobigeon, N., Parente, M., Du, Q., Gader, P., Chanussot, J., 2012. Hyperspectral Unmixing Overview: Geometrical, Statistical, and Sparse Regression-Based Approaches. IEEE J. Sel. Top. Appl. Earth Obs. Remote Sens. 5, 354–379. https://doi.org/10.1109/JSTARS.2012.2194696

Brell, M., Rogass, C., Segl, K., Bookhagen, B., Guanter, L., 2016. Improving Sensor Fusion: A Parametric Method for the Geometric Coalignment of Airborne Hyperspectral and Lidar Data. IEEE Trans. Geosci. Remote Sens. 54, 3460–3474. https://doi.org/10.1109/TGRS.2016.2518930

Brell, M., Segl, K., Guanter, L., Bookhagen, B., 2017. Hyperspectral and Lidar Intensity Data Fusion: A Framework for the Rigorous Correction of Illumination, Anisotropic Effects, and Cross Calibration. IEEE Trans. Geosci. Remote Sens. 55, 2799–2810. https://doi.org/10.1109/TGRS.2017.2654516

Briese, C., Pfennigbauer, M., Lehner, H., Ullrich, A., Wagner, W., Pfeifer, N., 2012. Radiometric calibration of multi-wavelength airborne laser scanning data. ISPRS Ann Photogramm Remote Sens. Spat Inf Sci 1, 335–340.

Buckley, S.J., Kurz, T.H., Howell, J.A., Schneider, D., 2013. Terrestrial lidar and hyperspectral data fusion products for geological outcrop analysis. Comput. Geosci. 54, 249–258. https://doi.org/10.1016/j.cageo.2013.01.018

Buddenbaum, H., Seeling, S., Hill, J., 2013. Fusion of full-waveform lidar and imaging spectroscopy remote sensing data for the characterization of forest stands. Int. J. Remote Sens. 34, 4511–4524. https://doi.org/10.1080/01431161.2013.776721

Chang, C.-C., Lin, C.-J., 2011. LIBSVM: a library for support vector machines. ACM Trans. Intell. Syst. Technol. TIST 2, 27.

Clark, M., Roberts, D., Clark, D., 2005. Hyperspectral discrimination of tropical rain forest tree species at leaf to crown scales. Remote Sens. Environ. 96, 375–398. https://doi.org/10.1016/j.rse.2005.03.009

Clark, M.L., Roberts, D.A., Ewel, J.J., Clark, D.B., 2011. Estimation of tropical rain forest aboveground biomass with small-footprint lidar and hyperspectral sensors. Remote Sens. Environ. 115, 2931–2942. https://doi.org/10.1016/j.rse.2010.08.029

Clasen, A., Somers, B., Pipkins, K., Tits, L., Segl, K., Brell, M., Kleinschmit, B., Spengler, D., Lausch, A., Förster, M., 2015. Spectral Unmixing of Forest Crown Components at Close Range, Airborne and Simulated Sentinel-2 and EnMAP Spectral Imaging Scale. Remote Sens. 7, 15361–15387. https://doi.org/10.3390/rs71115361

Cook, B.D., Corp, L.A., Nelson, R.F., Middleton, E.M., Morton, D.C., McCorkel, J.T., Masek, J.G., Ranson, K.J., Ly, V., Montesano, P.M., 2013. NASA Goddard's LiDAR, Hyperspectral and Thermal (G-LiHT) Airborne Imager. Remote Sens. 5, 4045–4066. https://doi.org/10.3390/rs5084045

Dai, W., Yang, B., Dong, Z., Shaker, A., 2018. A new method for 3D individual tree extraction using multispectral airborne LiDAR point clouds. ISPRS J. Photogramm. Remote Sens. 144, 400–411. https://doi.org/10.1016/j.isprsjprs.2018.08.010

Dalponte, M., Bruzzone, L., Gianelle, D., 2012. Tree species classification in the Southern Alps based on the fusion of very high geometrical resolution multispectral/hyperspectral images and LiDAR data. Remote Sens. Environ. 123, 258–270. https://doi.org/10.1016/j.rse.2012.03.013

Dalponte, M., Bruzzone, L., Gianelle, D., 2008. Fusion of Hyperspectral and LIDAR Remote Sensing Data for Classification of Complex Forest Areas. IEEE Trans. Geosci. Remote Sens. 46, 1416–1427. https://doi.org/10.1109/TGRS.2008.916480

Dalponte, M., Ørka, H.O., Ene, L.T., Gobakken, T., Næsset, E., 2014. Tree crown delineation and tree species classification in boreal forests using hyperspectral and ALS data. Remote Sens. Environ. 140, 306–317. https://doi.org/10.1016/j.rse.2013.09.006

Dandois, J.P., Ellis, E.C., 2013. High spatial resolution three-dimensional mapping of vegetation spectral dynamics using computer vision. Remote Sens. Environ. 136, 259–276. https://doi.org/10.1016/j.rse.2013.04.005

Debes, C., Merentitis, A., Heremans, R., Hahn, J., Frangiadakis, N., Kasteren, T. van, Liao, W., Bellens, R., Pižurica, A., Gautama, S., Philips, W., Prasad, S., Du, Q., Pacifici, F., 2014. Hyperspectral and LiDAR Data Fusion: Outcome of the 2013 GRSS Data Fusion Contest. IEEE J. Sel. Top. Appl. Earth Obs. Remote Sens. 7, 2405–2418. https://doi.org/10.1109/JSTARS.2014.2305441

Douillard, B., Underwood, J., Kuntz, N., Vlaskine, V., Quadros, A., Morton, P., Frenkel, A., 2011. On the segmentation of 3D LIDAR point clouds, in: Robotics and Automation (ICRA), 2011 IEEE International Conference On. IEEE, pp. 2798–2805.

Eitel, J.U.H., Höfle, B., Vierling, L.A., Abellán, A., Asner, G.P., Deems, J.S., Glennie, C.L., Joerg, P.C., LeWinter, A.L., Magney, T.S., Mandlburger, G., Morton, D.C., Müller, J., Vierling, K.T., 2016. Beyond 3-D: The new spectrum of lidar applications for earth and ecological sciences. Remote Sens. Environ. 186, 372–392. https://doi.org/10.1016/j.rse.2016.08.018

Gorretta, N., Gomez, C., 2016. Spectral–Spatial Unmixing Approaches in Hyperspectral VNIR/SWIR Imaging, in: Data Handling in Science and Technology. Elsevier, pp. 579–611.

Guanter, L., Richter, R., Kaufmann, H., 2009. On the application of the MODTRAN4 atmospheric radiative transfer code to optical remote sensing. Int. J. Remote Sens. https://doi.org/10.1080/01431160802438555

Hakala, T., Suomalainen, J., Kaasalainen, S., Chen, Y., 2012. Full waveform hyperspectral LiDAR for terrestrial laser scanning. Opt. Express 20, 7119. https://doi.org/10.1364/OE.20.007119

Heiden, U., Heldens, W., Roessner, S., Segl, K., Esch, T., Mueller, A., 2012. Urban structure type characterization using hyperspectral remote sensing and height information. Landsc. Urban Plan. 105, 361–375. https://doi.org/10.1016/j.landurbplan.2012.01.001

Holmgren, J., Persson, Å., 2004. Identifying species of individual trees using airborne laser scanner. Remote Sens. Environ. 90, 415–423. https://doi.org/10.1016/S0034-4257(03)00140-8

Kampe, T.U., Johnson, B.R., Kuester, M.A., Keller, M., 2009. NEON: the first continental-scale ecological observatory with airborne remote sensing of vegetation canopy biochemistry and structure, in: SPIE Optical Engineering+ Applications. International Society for Optics and Photonics, pp. 745402–745402.

Kashani, A., Olsen, M., Parrish, C., Wilson, N., 2015. A Review of LIDAR Radiometric Processing: From Ad Hoc Intensity Correction to Rigorous Radiometric Calibration. Sensors 15, 28099–28128. https://doi.org/10.3390/s151128099

Lee, D.D., Seung, H.S., 2001. Algorithms for non-negative matrix factorization, in: Advances in Neural Information Processing Systems. pp. 556–562.

Loncan, L., de Almeida, L.B., Bioucas-Dias, J.M., Briottet, X., Chanussot, J., Dobigeon, N., Fabre, S., Liao, W., Licciardi, G.A., Simoes, M., Tourneret, J.-Y., Veganzones, M.A., Vivone, G., Wei, Q., Yokoya, N., 2015. Hyperspectral Pansharpening: A Review. IEEE Geosci. Remote Sens. Mag. 3, 27–46. https://doi.org/10.1109/MGRS.2015.2440094

Luo, S., Wang, C., Xi, X., Pan, F., Peng, D., Zou, J., Nie, S., Qin, H., 2017. Fusion of airborne LiDAR data and hyperspectral imagery for aboveground and belowground forest biomass estimation. Ecol. Indic. 73, 378–387. https://doi.org/10.1016/j.ecolind.2016.10.001

Man, Q., Dong, P., Guo, H., 2015. Pixel- and feature-level fusion of hyperspectral and lidar data for urban land-use classification. Int. J. Remote Sens. 36, 1618–1644. https://doi.org/10.1080/01431161.2015.1015657

Melgani, F., Bruzzone, L., 2004. Classification of hyperspectral remote sensing images with support vector machines. IEEE Trans. Geosci. Remote Sens. 42, 1778–1790. https://doi.org/10.1109/TGRS.2004.831865

Morsdorf, F., Kötz, B., Meier, E., Itten, K.I., Allgöwer, B., 2006. Estimation of LAI and fractional cover from small footprint airborne laser scanning data based on gap fraction. Remote Sens. Environ. 104, 50–61. https://doi.org/10.1016/j.rse.2006.04.019

Morsdorf, F., Meier, E., Allgöwer, B., Nüesch, D., 2003. Clustering in airborne laser scanning raw data for segmentation of single trees. Int. Arch. Photogramm. Remote Sens. Spat. Inf. Sci. 34, W13.

Näsi, R., Honkavaara, E., Lyytikäinen-Saarenmaa, P., Blomqvist, M., Litkey, P., Hakala, T., Viljanen, N., Kantola, T., Tanhuanpää, T., Holopainen, M., 2015. Using UAV-Based Photogrammetry and Hyperspectral Imaging for Mapping Bark Beetle Damage at Tree-Level. Remote Sens. 7, 15467–15493. https://doi.org/10.3390/rs71115467

Nevalainen, O., Honkavaara, E., Tuominen, S., Viljanen, N., Hakala, T., Yu, X., Hyyppä, J., Saari, H., Pölönen, I., Imai, N.N., Tommaselli, A.M.G., 2017. Individual Tree Detection and Classification with UAV-Based Photogrammetric Point Clouds and Hyperspectral Imaging. Remote Sens. 9, 185. https://doi.org/10.3390/rs9030185

Oliveira, R.A., Tommaselli, A.M.G., Honkavaara, E., 2019. Generating a hyperspectral digital surface model using a hyperspectral 2D frame camera. ISPRS J. Photogramm. Remote Sens. 147, 345–360. https://doi.org/10.1016/j.isprsjprs.2018.11.025

Roberts, D.A., Gardner, M., Church, R., Ustin, S., Scheer, G., Green, R.O., 1998. Mapping chaparral in the Santa Monica Mountains using multiple endmember spectral mixture models. Remote Sens. Environ. 65, 267–279.

Roessner, S., Segl, K., Heiden, U., Kaufmann, H., 2001. Automated differentiation of urban surfaces based on airborne hyperspectral imagery. IEEE Trans. Geosci. Remote Sens. 39, 1525–1532.

Rogge, D.M., Rivard, B., Zhang, J., Feng, J., 2006. Iterative Spectral Unmixing for Optimizing Per-Pixel Endmember Sets. IEEE Trans. Geosci. Remote Sens. 44, 3725–3736. https://doi.org/10.1109/TGRS.2006.881123

Rogge, D.M., Rivard, B., Zhang, J., Sanchez, A., Harris, J., Feng, J., 2007. Integration of spatial–spectral information for the improved extraction of endmembers. Remote Sens. Environ. 110, 287–303. https://doi.org/10.1016/j.rse.2007.02.019

Sankey, T., Donager, J., McVay, J., Sankey, J.B., 2017. UAV lidar and hyperspectral fusion for forest monitoring in the southwestern USA. Remote Sens. Environ. 195, 30–43. https://doi.org/10.1016/j.rse.2017.04.007

Shi, C., Wang, L., 2014. Incorporating spatial information in spectral unmixing: A review. Remote Sens. Environ. 149, 70–87. https://doi.org/10.1016/j.rse.2014.03.034

Suomalainen, J., Hakala, T., Kaartinen, H., Räikkönen, E., Kaasalainen, S., 2011. Demonstration of a virtual active hyperspectral LiDAR in automated point cloud classification. ISPRS J. Photogramm. Remote Sens. 66, 637–641. https://doi.org/10.1016/j.isprsjprs.2011.04.002

Thomas, C., Ranchin, T., Wald, L., Chanussot, J., 2008. Synthesis of Multispectral Images to High Spatial Resolution: A Critical Review of Fusion Methods Based on Remote Sensing Physics. IEEE Trans. Geosci. Remote Sens. 46, 1301–1312. https://doi.org/10.1109/TGRS.2007.912448

Torabzadeh, H., Morsdorf, F., Schaepman, M.E., 2014. Fusion of imaging spectroscopy and airborne laser scanning data for characterization of forest ecosystems – A review. ISPRS J. Photogramm. Remote Sens. 97, 25–35. https://doi.org/10.1016/j.isprsjprs.2014.08.001

Vauhkonen, J., Hakala, T., Suomalainen, J., Kaasalainen, S., Nevalainen, O., Vastaranta, M., Holopainen, M., Hyyppä, J., 2013. Classification of Spruce and Pine Trees Using Active Hyperspectral LiDAR. IEEE Geosci. Remote Sens. Lett. 10, 1138–1141. https://doi.org/10.1109/LGRS.2012.2232278

Vivone, G., Alparone, L., Chanussot, J., Dalla Mura, M., Garzelli, A., Licciardi, G.A., Restaino, R., Wald, L., 2015. A Critical Comparison Among Pansharpening Algorithms. IEEE Trans. Geosci. Remote Sens. 53, 2565–2586. https://doi.org/10.1109/TGRS.2014.2361734

Wagner, W., 2010. Radiometric calibration of small-footprint full-waveform airborne laser scanner measurements: Basic physical concepts. ISPRS J. Photogramm. Remote Sens. 65, 505–513. https://doi.org/10.1016/j.isprsjprs.2010.06.007

Wang, L., Shi, C., Diao, C., Ji, W., Yin, D., 2016. A survey of methods incorporating spatial information in image classification and spectral unmixing. Int. J. Remote Sens. 37, 3870–3910. https://doi.org/10.1080/01431161.2016.1204032

Yokoya, N., Yairi, T., Iwasaki, A., 2012. Coupled Nonnegative Matrix Factorization Unmixing for Hyperspectral and Multispectral Data Fusion. IEEE Trans. Geosci. Remote Sens. 50, 528–537. https://doi.org/10.1109/TGRS.2011.2161320

Zou, X., Zhao, G., Li, J., Yang, Y., Fang, Y., 2016. 3D LAND COVER CLASSIFICATION BASED ON MULTISPECTRAL LIDAR POINT CLOUDS. ISPRS - Int. Arch. Photogramm. Remote Sens. Spat. Inf. Sci. XLI-B1, 741–747. https://doi.org/10.5194/isprsarchives-XLI-B1-741-2016